Study of Real-Time Spatial and Temporal Behavior of Bacterial Biofilms Using 2D Impedance Spectroscopy

Caleb Begly, *Member, IEEE,* David Ackart, Julian Mylius, Randall Basaraba, Adam J. Chicco, and Thomas W. Chen, *Senior Member, IEEE*

Abstract*—*Objective: **The purpose of this paper is to demonstrate the use of 2D impedance spectroscopy to identify areas of biofilm growth on a CMOS biosensor microelectrode-array.** ***Methods:*** **This paper presents the design and use of a novel multichannel impedance spectroscopy instrument to allow 2D spatial and temporal evaluation of biofilm growth. The custom-designed circuits can provide a wide range of frequencies ($1\,\mathrm{Hz} - 100\,\mathrm{kHz}$) to allow customization of impedance measurements, as the frequency of interest varies based on the type and state of biofilm under measurement. The device is capable of taking measurements as fast as once per second on the entire set of impedance sensors, allowing real-time observation. It also supports adjustable stimulus voltages. The distance between neighboring sensors is 220 micrometers which provides reasonable spatial resolution for biofilm study.** ***Results:*** **Biofilm was grown on the surface of the chip, occupancy was measured using the new tool, and the results were validated optically using fluorescent staining. The results show that the developed tool can be used to determine the bacterial biofilm presence at a given location.** ***Conclusion:*** **This paper confirms that 2D impedance spectroscopy can be used to measure biofilm occupancy. The new tool developed to perform the measurements was able to display real-time results, and determine biofilm coverage of the array electrodes.** ***Significance:*** **The system presented in this report is the first fully integrated 2D EIS measurement system with full software support for capturing biofilm growth dynamics in real-time. Due to its ability to nondestructively monitor biofilms over time, 2D impedance spectroscopy using a microelectrode-array is a useful tool for studying biofilms.**

***Index Terms*—Electrochemical impedance spectroscopy, CMOS technology, Real-time, 2D, Multichannel, Biofilm**

Manuscript submitted Feburary 21, 2020

Results presented in this paper are based upon collaborative work supported by a National Science Foundation NRT Grant No. 1450032. Any opinions, findings, conclusions or recommendations expressed in this paper are those of the author(s) and do not necessarily reflect the views of the National Science Foundation.

This work was also supported in part by National Science Foundation grant GDE-0841259.

C. Begly and T. Chen are with the Department of Electrical and Computer Engineering, Walter Scott Jr. College of Engineering, Colorado State University, Fort Collins, CO, USA. T. Chen is also with School of Biomedical Engineering, Walter Scott Jr. College of Engineering, Colorado State University, Fort Collins, CO, USA (correspondence e-mail: chen@colostate.edu)

D. Ackart, J. Mylius, and R. Basaraba are with the Department of Microbiology, Immunology and Pathology, College of Veterinary Medicine and Biomedical Sciences, Colorado State University, Fort Collins, CO, USA

A. Chicco is with the Department of Biomedical Sciences, College of Veterinary Medicine and Biomedical Sciences, Colorado State University, Fort Collins, CO, USA

I. Introduction

The study of biofilms and their effect on disease treatment, prevention, and cures has been increasing in importance in recent years. Back in 2002, the NIH turned its sights on biofilms, stating that at the time over 80% of microbial infections were associated with biofilms in the body[1]. Among the goals were the desire to develop instruments or techniques capable of non-destructive, real-time, three dimensional monitoring of biofilms. Steady increases in antibiotic resistant bacteria deaths year-over-year, have made the study of biofilms more urgent now than in the previous two decades.

A. Biofilm Background

Bacterial biofilms are colony formations developed by bacteria that allow them to anchor onto a surface, and survive hostile environments. In the lifecycle of a bacterial biofilm, free floating (planktonic) bacteria anchor onto a surface and then secrete extracellular polysacharides (EPS) which form a slimy residence for the new colony to grow and thrive in, eventually reaching a mature colony size[2]. At this point, the colony will continue to release planktonic bacteria into the surrounding environment from the outer surface of the biofilm[2].

The formation of harmful bacteria biofilms on some surfaces can be troublesome, particularly in the case of medical implants. Once a biofilm forms on an implant, the biofilm will continue to harbor the infection, distributing planktonic bacteria into the surrounding environment[2]. The EPS matrix shields the cells inside from hostile environments, and limits the effect of treatments. Antibiotic treatments are generally ineffective alone because they only impact the free floating bacteria and bacteria on the very surface of the biofilm. Instead, either high-dose, long term antibiotic treatment is needed to give the antibiotic ample opportunity to penetrate the biofilm, or the implant must be removed[1], [2].

B. Antibiotic Resistant Concerns

Adding to the need to study and understand biofilms is the increase in antibiotic resistant bacteria. The NIH noted in its proposal for studying biofilms that bacteria in biofilms can have higher antibiotic resistance naturally (due to EPS shielding) and they increase the likelihood of gene transfer[1]. The long, high-dose antibiotic treatments needed to get rid of,

or suppress biofilms further increase the likelihood of selecting antibiotic resistant strains over the course of the treatment.

There is a general, and concerning increase in drug-resistant infections over time. Over seven hundred thousand people currently die each year from antimicrobial resistant disease, and that figure is expected to increase to ten million by 2050, finally eclipsing cancer as the number one cause of death[3]. A summary report from the UK Review on Anti-Microbial Resistance recommends reduction of unnecessary use of antibiotics, development of better diagnostics, and development of alternatives as ways to combat the increase in drug-resistant deaths[4], however there is still a need for new tools to allow studying drug-resistant strains so new treatments can be developed.

Among the causes of deaths due to bacteria, *Mycobacterium tuberculosis* (TB) stands out as a large and continuing problem. As of 2014, it accounts for 1.5 million deaths annually, and the multidrug-resistant variants of TB kill two hundred thousand people annually - 28.6% of all deaths due to anti-microbial resistant infections[4]. In this paper we use *Mycobacterium smegmatis* to validate the capabilities of our device. This was chosen because it is a common model for studying *M. tuberculosis*, although there are some limitations[5].

C. Current Solutions

There is already some progress in finding alternatives to antibiotics in the case of medical implants. Surface structure treatments, and novel materials can provide good alternative to the current practice of antibiotic treatment of medical implants (antibiotic catheter lock therapy and antibiotic coatings)[2]. New materials like metal-organic framework (MOF) containing substances have been shown to be effective at preventing biofilm formation of *Pseudomonas aeruginosa* without the use of antibiotics[6]. These new materials help reduce the problem of biofilm formation on new implants, but there is still a need to study biofilms for management and removal of biofilms in existing situations, or in tough cases where the biofilm forms on the surfaces of other organs. For example, some *P. aeruginosa* strains form biofilms on the surface of lung tissue[7]).

Electrochemical impedance spectroscopy (EIS) has been used as a technique for real-time monitoring of biofilms in many applications, due to its ability to measure characteristics of the biofilm without damaging the cells[8]. The technique involves applying a small stimulus voltage ($5-100\,mV_{pp}$) over a range of frequencies (up to 100 kHz) to the system, and then measuring the current over a wide range of frequencies to measure the resistance between two electrodes where biofilm may grow[9], [10], [11], [12], [13], [14], [15], [16]. By keeping the stimulus small, the system can measure the response in the pseudo-linear range, and avoid any substantial disruption to the specimen or solution[17]. Some of the promising approaches so far involve growing the biofilm on a macro electrode, and then monitoring the change in EIS[9], [10], [11], [12], [13].

While these approaches demonstrate how EIS can be used with good temporal resolution, developing a measurement system that has 2D spatial resolution is more challenging. A 2005 project used a combination optical and microelectrode EIS probe to get spatial information by using a motorized stage to scan the probe over the surface of a biofilm grown on a macroelectrode[18]. A similar 2013 project used a conductive atomic force microscopy (AFM) tip to perform a 2D EIS scan of the biofilm[19]. Both techniques gave good spatial resolution, but sacrificed temporal resolution[1]. In addition, moving a probe through the solution above a biofilm has the potential to disrupt the biofilm while the measurement is being taken.

To allow for measurements with high spatial resolution as well as temporal resolution, a microelectrode array can be used. A 2012 project used a 96×96 electrode array (9216 electrodes) developed using a CMOS process to measure EIS in a 2D plane[14]. It has lower spatial resolution ($\approx 17\,\mu m$ versus $\approx 1\,\mu m$) but potentially improves temporal resolution over the scanned modes [14], [19]. Measurements were taken using an external LCR meter, limiting the portability and volumetric density of the device compared to other designs.

Another 2D electrode array design was attempted and featured a 10x10 electrode array developed using a CMOS process[20]. The electrodes on this chip are round with a diameter of $100\,\mu m$, and a pitch of $\approx 150\,\mu m$ [20][2]. Similar to the other example[14], this device uses a separate reference/counter electrode so the EIS measurements are taken vertically[20]. While the spatial resolution is less than other approaches, this chip includes a built-in frequency synthesizer and readout, making it potentially more compact, however readouts from the chip were still performed using an external data acquisition card.

The above mentioned approaches used plain disk[18], [20] or disk analogue[14] microelectrodes, however interdigitated electrodes (IDEs) can be used to measure effects closer to the surface of the electrode. This is useful when looking at effects like biofilms bonding to the surface of the electrode. Using an width-to-gap ratio on the IDE array of 3:4, 90% of the total electric field strength can be found within $5\,\mu m$ of the surface of the electrodes[21]. It was also noted that the number of fingers doesn't impact the signal to noise ratio significantly because the background noise is "proportional to the area of the electrodes only", but "signal value is proportional to the area of the whole array" and increasing the number of fingers increases both [21].

Using IDEs, Paredes et. al. [22] designed a silicon-based small chip that can be inserted into one well of a 96-well microtiter plate for impedance measurements using a benchtop impedance analyzer over a range of stimulus frequencies. Their results showed the noticeable change in impedance between the interdigitated electrodes during a 20-hour biofilm culture period, especially over the lower frequency range of stimulus frequencies. However, their experiment setup only allowed one set of IDEs per well, thus providing no spatial information about biofilm growth. The use of the benchtop impedance analyzer for measurements does not render an

[1]The exact reduction in temporal resolution for both papers is unknown since the paper didn't include the scan time.

[2]Exact pitch isn't provided; instead it is estimated from Figure 7.

integrated approach that would facilitate an array of electrodes. More recently, Subramanian et. al. [23] demonstrated the use of IDEs on glass substrate for measuring the formation of *E. coli* biofilm. A benchtop potentiostat was used for EIS measurement every 10-15 minutes during the biofilm growth. Furthermore, this approach also reported a procedure for biofilm treatment using a feedback control loop from the sensor output using the bioelectric effect (BE). However, similar to the approach in [22], this approach provides one set of IDEs per measurement site with no spatial information about biofilm growth. The approach aimed at giving a threshold indication of biofilm presence for activating the BE treatment. The overall instrumentation setup using benchtop potentiostat did not lend itself to a highly integrated design that could support IDE arrays. Huiszoon et. al. [24] applied the EIS approach in [23] to detecting and treating biofilms in a urinary catheter by creating one set of IDEs on flexible polyimide substrate. A similar biofilm treatment method using BE was also used to demonstrate its effectiveness. Using an external benchtop potentiostat for EIS measurement, the measurement aimed for the same threshold activation of biofilm treatment using the BE method.

When measuring EIS, two general approaches are used, specifically looking at the spectrum with or without phase information. A 2012 review of using impedance analysis for microbial electrochemical systems noted that, without phase information, the impedance modulus interpretation is "less sensitive to system parameters", while still providing the important information [17]. Fitting models with higher component counts can lead to overfitting, and masking the underlying effect. The information included in the phase is often not useful when looking at biofilm density[18]. Finally, the systems can be measured using capacitors and resistors only in an idealized EIS circuit model, so the phase information is redundant. For experiments presented in this paper, we used the impedance modulus spectrum.

The system presented in this report is the first fully integrated 2D EIS measurement system with full software support for capturing biofilm growth dynamics in real-time. The goal is to provide a flexible tool for studying various aspects of biofilms. The tool provides 80 $55\,\mu m \times 55\,\mu m$ electrodes with a pitch of $220\,\mu m$, and a temporal resolution of $1.23\,ms$ per channel per frequency. The system allows full control of the trade-off between frequency resolution and temporal resolution. For example, a user could monitor only one frequency with a temporal resolution of $10.1\,SPS$, or they could get a 10 frequency spectrum with a temporal resolution of $1.01\,SPS$. This flexibility allows this platform to be used for a broad range of applications, each with different requirements. Monitoring biofilm in real-time is essential in providing better understanding of biofilm formation, growth, and its interactions with therapeutics. Providing an integrated system solution will allow faster evaluation of drug efficacy to combat biofilm formation.

This system improves on the existing solutions in several ways. Because the whole system is integrated and compact, it allows monitoring the biofilm formation and growth while inside an incubator over a long period of time. This integrated approach avoids the disturbance of connecting external benchtop instruments for measurement, or removing the sample from the incubator each time a measurement is needed. The independent trans-impedance amplifiers (TIAs) on each channel improve on designs that constantly switch between electrodes when muxing channels down. These switching transients constantly connect and disconnect the electrochemical cells resulting in longer settling times, and potentially disturbing the sample. By providing each channel its own amplifier, the switching is done on the post-amplified signal, minimizing the impact on the state of the electrochemical cell[25]. Finally, because the platform integrates multiple measurement modalities including the one discussed in this paper, the user has additional flexibility when studying biofilms without the need to swap measurement devices manually.

This paper is organized as follows: Section II-A presents an overview of the existing Electrochemical Biosensor System platform and how the new Impedance Spectroscopy Instrument add-on fits into the system plan. Section II-B discusses the electronics design for the PCB including the instrumentation theory and design choices. The graphical user interface (GUI), measurement algorithms, driver libraries, and other software are covered in Section II-C. The methods for design validation are detailed in Section II-D. Results are presented in Section III and discussed in Section IV. Finally, the conclusions are summarized in Section V.

II. Materials and Methods

A. Overall System Design

A highly integrated CMOS microelectrode-array (MEA) biosensor platform developed previously at CSU[26] can be used for a variety of electrochemical experiments. The chip, shown in Fig. 1 has 16k electrodes available for amperometry imaging, and 80 pairs of IDEs for impedance spectroscopy. This paper presents the new custom-designed impedance spectroscopy instrument which works directly with the CMOS biosensor system to add impedance spectroscopy features to the platform.

The full Electrochemical Biosensor System platform is shown in Fig. 1 (a) and consists of a main board and additional add-on boards in a stack. The system plugs into a computer via USB, and is controlled with a software interface. New chips can be inserted into the socket, and then samples can be grown on the surface of the chip. The entire device is small ($100\,mm \times 100\,mm$ footprint) to allow the entire integrated device to be placed into an environmental chamber if needed.

As shown in Fig. 2, the add-on impedance spectroscopy instrument consists primarily of a stimulus generation part, and a readout part, with some level shifting and scaling built in. The stimulus is provided to all the channels which are modeled as the device under test (DUT) and the outputs are read by dedicated transimpedance amplifiers (TIAs). The outputs from the TIAs are then multiplexed down so they can be read out using a single analog to digital converter (ADC). To operate the $1\,MHz$, 14-bit resolution ADC needed to sample the signal with the desired speed and quality, the digital SPI-compatible interface operates at a bit rate of $16\,Mbps$.

This article has been accepted for publication in a future issue of this journal, but has not been fully edited. Content may change prior to final publication. Citation information: DOI 10.1109/TBCAS.2020.3011918, IEEE Transactions on Biomedical Circuits and Systems

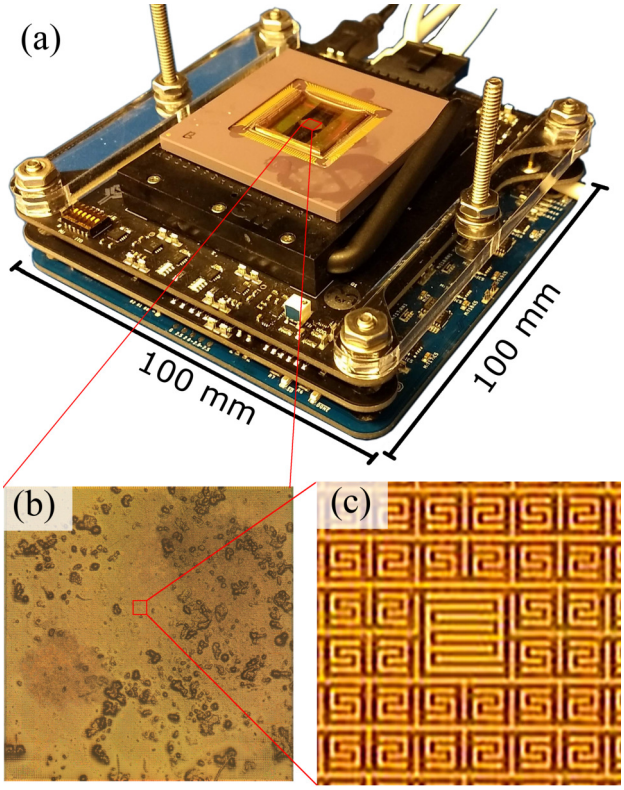

Fig. 1: **Overall platform with area detail callouts.** (a) Assembled Electrochemical Biosensor System including new add-on impedance spectroscopy board (blue board on the bottom). (b) Closeup of full $2.2\,mm \times 2.2\,mm$ EIS array chip surface with biofilm growth. (c) Closeup of a single EIS electrode on the array.

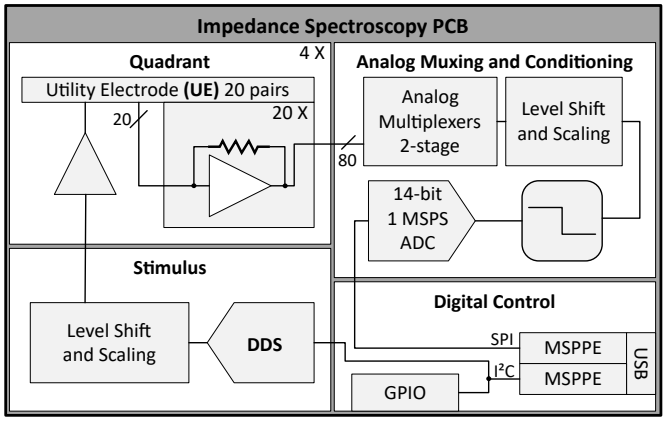

Fig. 2: **Block diagram for Impedance Spectroscopy Instrument add-on board.** The existing Electrochemical Biosensor System exposes the 80 pairs of on-chip utility electrodes (20 pairs per quadrant) that are used by this add-on [26].

B. Electrical System Design

The impedance spectroscopy instrument consists of the custom instrumentation board shown in Fig. 3. This board is designed to work as an add-on to the existing Electrochemical Biosensor System platform, and it simply plugs into the bottom of the existing device. User control is provided by

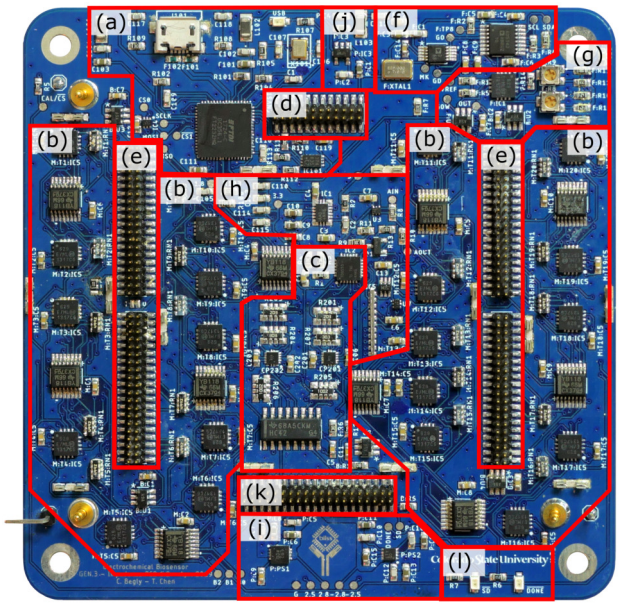

Fig. 3: **Impedance Spectroscopy Board breakdown.** (a) USB connection and controller chip, (b) Transimpedance amplifiers and Muxing, (c) Digital control logic and level translation, (d) Communication connection to existing system, (e) Connections to utility electrodes on existing system, (f) Stimulus generation, (g) Analog stimulus level shifting and scaling, (h) Analog result level shifting, filtering, and sampling, (i) Analog power conditioning, (j) Digital power conditioning, (k) Power supply connector (from existing system), (l) Indicator LEDs

connecting the device to a computer using the USB port on the side. The following subsections discuss the theory, design, and operation of this board.

1) Function Generation: The stimulus signal for EIS is a single frequency, low amplitude sinusoid, where the frequency can be swept over a wide frequency range. For the frequency generation, we use the AD9833 direct digital synthesis (DDS) chip which is capable of generating a fixed amplitude sine wave output from with a maximum frequency resolution of $0.1\,Hz$[3]. The EIS frequency range of interest varies depending on the application [14], [16], [15], [20], [19], [13], [12], [11], [27], [18], [10]. Our design focuses on the window from $1\,kHz$ to $100\,kHz$ which falls well within the capability of this chip. The chip is controlled directly via the serial-peripheral interface (SPI). The other benefit of this chip is that it is free-running so no CPU time or USB bandwidth is needed to control stimulus generation once it is running.

2) Stimulus Level-Shifting and Scaling: The output of the DDS chip is a fixed $600\,mV_{pp}$ sine wave with an offset of $325\,mV$ from ground. When applying the signal to the electrodes, the signal mean must be at zero to prevent or reduce drift over time. Similarly, the stimulus voltage must be small $(5 - 100\,mV_{pp})$ so the biofilm is not damaged[11], [13], [14], and the system operates in the pseudo-linear region of the electrochemical system[17]. This prevents substantial oxida-

[3]Using a $25\,MHz$ master clock

This article has been accepted for publication in a future issue of this journal, but has not been fully edited. Content may change prior to final publication. Citation information: DOI 10.1109/TBCAS.2020.3011918, IEEE Transactions on Biomedical Circuits and Systems

tion or reduction products and allows measuring the system impedance magnitude (modulus) at the stimulus frequency.

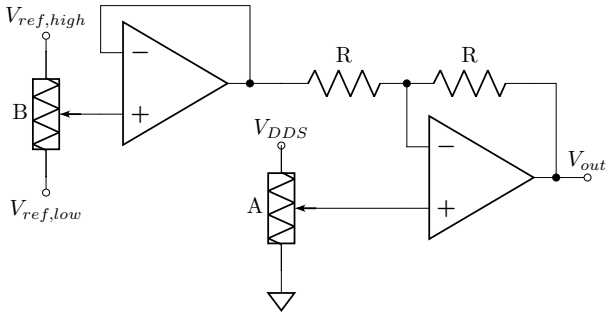

Fig. 4: **Stimulus Level-Shift and Scale Circuit.** This takes the generated waveform from the output of the direct digital synthesis (DDS) chip and allows it to be programmatically scaled to the desired amplitude and offset using the digital potentiometers, A and B.

To take this fixed output signal and tailor it to the desired output amplitude and offset, the signal is passed through an adjustable level shift and scale system. The circuit to do this is shown in Fig. 4 and uses a dual-channel digital potentiometer (digipot) and four operational amplifiers (op amps). The digital synthesis output is passed into digipot A which scales it down by the factor $\frac{A}{256}$ where A is some value between 0 and 255. The output then buffers and scales this, and subtracts V_{ref}. The resulting output is shown in (1).

$$\begin{aligned} V_{out} &= 2 \cdot \frac{A}{256} \cdot V_{DDS} - V_{ref} \\ &= A \cdot \frac{V_{DDS}}{128} - V_{ref} \end{aligned} \tag{1}$$

The design also has a tunable offset to allow shifting the DC center of the signal from $325\,mV$ down to $0\,V$. This allows flexibility in stimulus, while still providing enough precision to avoid large DC offsets during normal EIS operation. Digipot B selects a value between its high and low sides, allowing subtraction of a programmable offset in that range. The output is then buffered and used as V_{ref}. The value of V_{ref} can be estimated as shown in (2).

$$V_{ref} = B \cdot \left(\frac{V_{ref,high} - V_{ref,low}}{256} \right) + V_{ref,low} \tag{2}$$

$V_{ref,high}$ and $V_{ref,low}$ are carefully chosen so that, when the digipots are programmed to the same value ($A = B$), the mean of the output signal is zero. The nominal values for these reference voltages are computed using (2) and (1) such that the offset is shifted to 0 whenever A=B. The calculated values are shown in (3).

$$\begin{aligned} V_{ref,low} &= \mathbf{0} \\ V_{ref,high} &= 256 \cdot \frac{325\,mV}{128} = \mathbf{650\,mV} \end{aligned} \tag{3}$$

In practice, variations in components and buffer offsets result in true values that differs slightly from the computed values and need fine adjustment on a per-device basis. To provide this adjustment, both $V_{ref,high}$ and $V_{ref,low}$ are generated using the buffered output from a trim potentiometer (trim pot) network as shown in Fig. 5. During calibration, these potentiometers are adjusted until the output has exactly a zero mean at the two extremes of A and B. In order to make tuning easier without overshooting, R_1 through R_4 are used to reduce tuning sensitivity. The resulting design makes $V_{ref,low}$ and $V_{ref,high}$ adjustable from $-100\,mV$ to $100\,mV$ and from $489\,mV$ to $689\,mV$ respectively. These tuning ranges provide plenty of granularity and make the calibration easier as expected. The complete calibration steps and results are discussed in Section III-A.

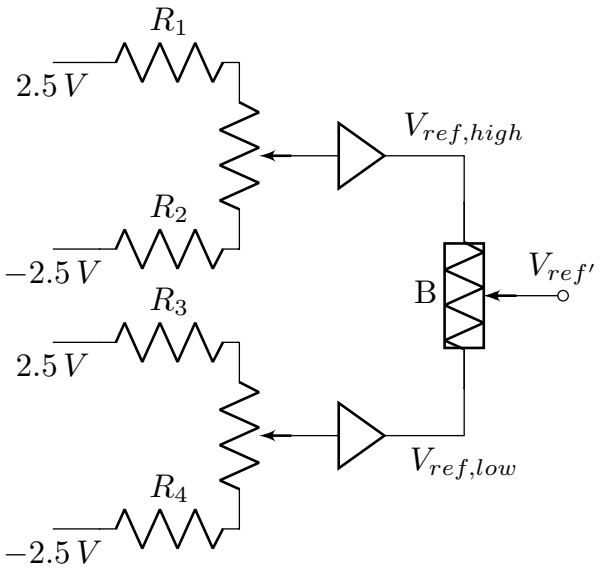

Fig. 5: **Tuning Potentiometer Network.** The potentiometers with series resistors allow calibrating $V_{ref,high}$ and $V_{ref,low}$ so digipot B can select reference values from the correct range.

3) Transimpedance Amplifier: Once the stimulus signal has been prepared, it needs to be applied to each channel, and the sensor output current recorded. This is done using a two-electrode system as shown in Fig. 6.

The stimulus voltage is fanned out to four buffers (one for each quadrant of the device) and then these are connected to one side of the electrodes. R_1 and R_2 represent the non-ideal resistances in the connection to the device under test, and are low in value. The stimulus across the device under test is slightly less than V_{stim} as shown in (4), and the error percentage is shown in (5). These equations show that as long as $R_{dut} \gg R_1 + R_2$ the error is small and tends towards zero.

$$V_{dut} = V_{stim} \cdot \frac{R_{dut}}{R_{dut} + R_1 + R_2} \tag{4}$$

$$\%\,error = \frac{R_1 + R_2}{R_{dut} + R_1 + R_2} \cdot 100 \tag{5}$$

The transimpedance amplifier (TIA) in the readout part of each channel holds the working electrode at a virtual ground (or near it, subject to R2) and converts the current to an output voltage as shown in (6). Once V_{in} is known, the resistance of

This article has been accepted for publication in a future issue of this journal, but has not been fully edited. Content may change prior to final publication. Citation information: DOI 10.1109/TBCAS.2020.3011918, IEEE Transactions on Biomedical Circuits and Systems

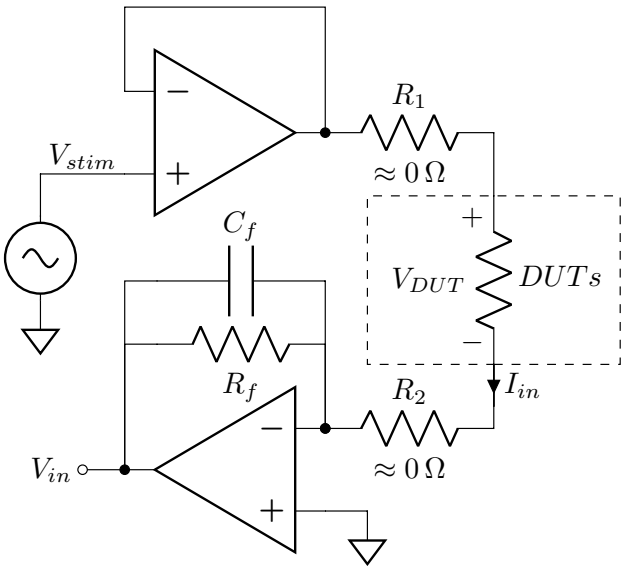

Fig. 6: **Channel Stimulus and TIA Readout.** This diagram shows how stimulus is applied to a device under test, and how the resulting current is read out using a transimpedance amplifier.

the DUT is computed as shown in (7). As expected, as long as $R_1 + R_2$ is small, the error is small.

$$V_{in} = -I_{in} \cdot R_f \tag{6}$$

$$R_{dut} = -\frac{V_{stim}}{V_{in}} \cdot R_f - R_1 - R_2 \tag{7}$$

The feedback capacitor C_f helps with stability and noise reduction by acting in conjunction with R_f as a low-pass filter with a corner frequency of $\frac{1}{2\pi R_f C_f}$. A lower corner frequency means less noise is passed through, and blocks interference, but there is some attenuation close to the corner frequency. This trade-off between noise reduction and gain is discussed more in Section II-B6.

4) MUX: Each of the eighty channels has a dedicated TIA, and then the outputs are multiplexed down in two stages to a single shared analog-to-digital converter (ADC). Ten 8:1 muxes (TS5N118DBQR) are used to take blocks of 8 channels down to 10 block signals. The outputs of these are then shorted together, and the enables on the muxes are chosen so only one output is enabled at a time. The muxes are rail-to-rail analog muxes with a bandwidth of $25\,MHz$.

There is also a 2:1 MUX that chooses between V_{int} and V_{ext} before the Level-Shifting and Scaling stage to allow this system to sample external voltage signals. It allows integrated sampling of the existing system, and is used during the automated system calibration to sample the stimulus signals.

5) Input Level-Shifting and Scaling: The input to the system needs to be scaled from the $\pm 2.5\,V$ dual-rail side to the $0 - 2.5\,V$ range of the ADC. This involves scaling it down by a factor of 2 and shifting it up by $1.25\,V$ and is done using an inverting amplifier with a non-zero reference. This circuit gives the desired V_{out} as shown in (8)

$$V_{out} = -\frac{1}{2}V_{in} + 1.25 \tag{8}$$

6) ADC: To sample the signals, the ADC must be capable of sampling more than twice as fast as the highest frequency component in the signal. The ADC used is the MAX11195 14-bit ADC capable of up to $2\,MSPS$ which has a SPI-compatible interface. Since the highest desired signal frequency in our system is $100\,kHz$, the Nyquist frequency is $200\,kHz$ and sampling will have to be faster than that to avoid aliasing. An RC anti-aliasing filter is placed in front of the ADC to attenuate higher frequency noise. In practice, a perfect anti-aliasing filter is not possible (and a single-pole RC filter isn't close), so by oversampling by 10x, we allow for a $400\,kHz$ transition band $\left(\frac{1\,MHz}{2} - 100\,kHz = 400\,kHz\right)$. The frequency dependent gain is shown in (9).

$$|A| = \sqrt{\frac{1}{1 + (2\pi f RC)^2}} \tag{9}$$

From this we can choose the anti-aliasing filter by how close we can get to our maximum frequency without introducing too much gain error. For example, with $R = 7.5\,\Omega$ and maximum allowed gain error of 1% at $100\,kHz$, C must be less than $30.24\,nF$ ($f_c \geq 702\,kHz$). Using the manufacturer recommended $1\,nF$ capacitor, drops the error to $< 0.001\,\%$ but increases the amount of noise that is let through.

7) USB Interface and Digital Control: All control logic is handled by a USB interface chip from FTDI which provides two Multi-Protocol Synchronous Serial Engine (MPSSE) channels over USB. One channel is configured to SPI serial, and the other is configured as I^2C. All addressing and enable bits are handles by an I^2C controlled general purpose IO (GPIO) extender as shown in Fig. 7.

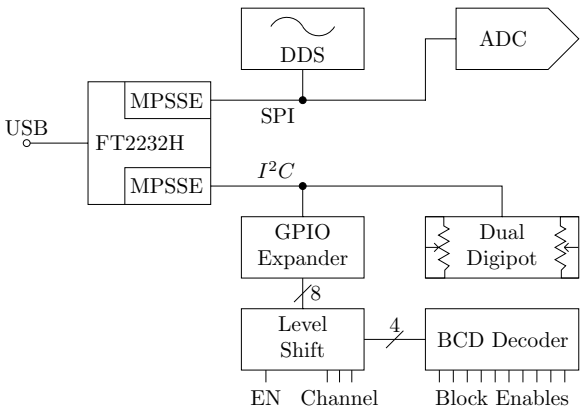

Fig. 7: **Digital Control Top-Level Diagram.** The FT2232H provides two MPSSE engines - one is configured for SPI and the other is used for various I^2C devices.

Three bits are used to select 1-of-8 on the muxes, and then 4 bits are passed through a binary coded decimal (BCD) converter to enable one of the 10 muxes at a time. This chip has a break-before-make design to ensure that only one MUX

is ever enabled at a time. A system enable bit is tied to the stimulus output, and defaults to OFF. This allows the software to fully configure the desired waveform before applying it to the system to avoid any undesired glitches or unknown states.

C. Software Design

1) Overview: The software for the device is written in C++, and consists of a base library overlaying the FTD2XX library, and a graphical user interface (GUI) written in Microsoft Foundation Classes (MFC) for easy user interaction. This logical arrangement was chosen to allow easier integration of the device into other applications or scripts as needed, so making things like a Matlab library or Python library would be easy.

The base library consists of a custom layer over the core FTD2XX library because the manufacturer provided library was too slow. For I^2C in the system, the slowdown was not a problem. However, driving the high-speed SPI line for the ADC was limited due to baked in timing constraints. Using the manufacturer provided LibMPSSE-SPI, the fastest possible sampling speed measured was approximately $340\,SPS$, limited mostly by that library's handling of the chip-select lines. Using the custom library, the maximum sampling speed was increased to $937.5\,kSPS$[4]. The library also includes objects that allow direct control over all chips connected to the FTDI chip, including the function generator, digipot, ADC, and GPIO chips.

2) User Interface: The User Interface is shown in Fig. 8. The user can operate any connected device, adjust the stimulus settings, and take impedance readings, spectrum readings, or raw readings. There are also tools for looking at the effect of stimulus voltage on the result, and for displaying a live (updated every 2 seconds) view of the heatmap. The user can click on any location on the image to get the exact value, and the data is also available in CSV format for further processing in Matlab, R, or Python.

3) Measurement Algorithms: Since the system functions by applying a sine wave to the system and then measuring the output sine wave to see how much the amplitude changed, accurate measurement of amplitude is important. A simple max/min difference algorithm is not ideal because noise in the system will typically make this an overestimate of peak-to-peak voltage, particularly at low amplitudes. The other problem is that it doesn't provide an estimate of how close to sinusoidal the output is which can be important for ruling out bad measurements or substantial interference. Instead, we use a linear least squares (LLS) fit. While this is computationally more intensive, it provides a high quality measurement, even at low SNR, provided the noise is normally distributed.

a) Frequency Measurement: To get a linear least squares fit, we first need to estimate the frequency of the measured sinusoid. There are several algorithms for this including fast Fourier transform (FFT), single-threshold zero-crossing detection (STZX), dual-threshold zero-crossing detection (DTZX), and single threshold zero-crossing detection with known frequency (STZX+). The comparison between these algorithms is shown in Table I.

[4]Assumes $12\,MHz$ master clock for the FT2232H chip

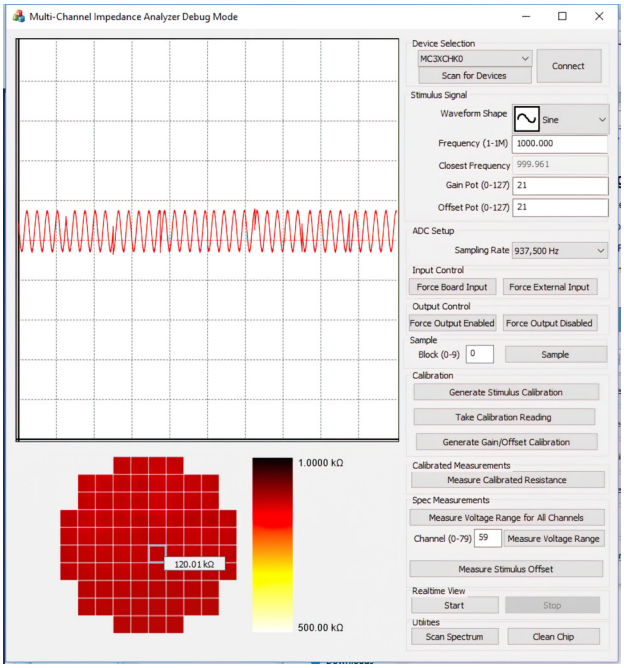

Fig. 8: **User Interface**. The large graphing area in the middle allows viewing, measuring, and exporting the directly sampled waveform data (when captured). The heatmap in the lower left provides a visual representation of the resistances on the surface of the chip. This updates in real-time when scanning so the user can see changes as they happen.

TABLE I: Comparison of Frequency Measurement Algorithms

Algorithm	Pros	Cons
FFT	Fast	Too inaccurate for linear least squares
STZX	Fast	Noise intolerant
DTZX	Good noise tolerance	Noise amplitude must be estimated
STZX+	Fast, good noise tolerance	Frequency must be estimated

Fast Fourier transform estimates are not useful for measuring the frequency to the exactness needed for LLS because the frequency resolution is limited to bin widths as shown in (10).

$$\Delta_f = \frac{F_s}{N}, \tag{10}$$

In our case ($F_s = 1\,MHz, N = 1000$) the frequency resolution is $1\,kHz$ which is too broad to be used. While spectrum interpolation can give a closer idea of where the frequency is, and increasing the number of points in the FFT can also help, these increase both the computational complexity and sampling time, while still giving results that are at best comparable to other techniques.

STZX is useful when looking at signals that are monotonically increasing on rising edges and monotonically decreasing on falling edges. This typically limits its use to signals which

This article has been accepted for publication in a future issue of this journal, but has not been fully edited. Content may change prior to final publication. Citation information: DOI 10.1109/TBCAS.2020.3011918, IEEE Transactions on Biomedical Circuits and Systems

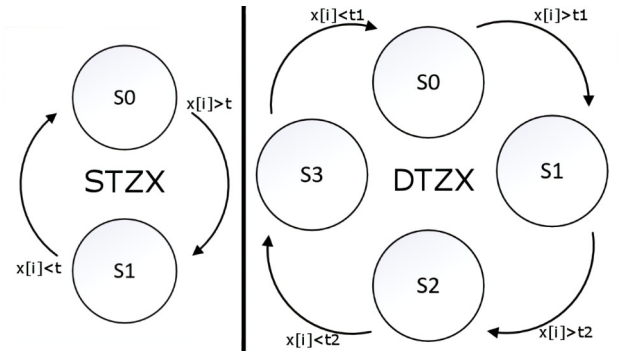

Fig. 9: **STZX and DTZX State Machines.** The addition of a second threshold to DTZX reduces sensitivity to noise.

have little noise, or smoothed signals. It operates by a simple state machine as shown in Fig. 9 that looks for rising and falling edges crossing some threshold in the middle of the signal, counting up the whole number of crossings (rising and falling pair), and then dividing the distance from the first crossing to the last crossing by the number of whole crossings to get the period of the signal. However, it fails when the noise causes the algorithm to detect many zero-crossings on the same edge. DTZX solves this problem by requiring the signal to cross two thresholds before registering a crossing. As long as the two thresholds are further apart than the expected maximum noise contribution, this algorithm is noise tolerant. This difference is shown in Fig. 10.

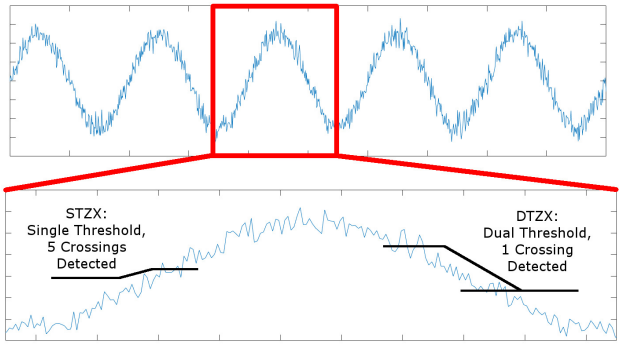

Fig. 10: **STZX and DTZX applied to a noisy sinusoid.** The single threshold without holdoff tends to overcount crossings due to fluctuations around the threshold. The dual threshold solves this by placing the two thresholds further apart than the expected noise fluctuations.

STZX+ is similar to STZX, but to deal with the possibility of multiple false crossings near a true crossing due to noise, STZX+ advances the algorithm by some minimum number of samples (jump distance) once a crossing is detected. Using a fixed jump distance like 10-20 samples can work OK for high frequency signals, but still fails on lower frequency signals because the slope is so shallow that the jump will not get far enough away. The optimal jump distance is 1/4 of a period of the signal because that goes from the crossing to either the next peak or valley which is maximally away from the threshold. This is why for STZX+ it is best to have an estimate of the frequency. Since this system applies the stimulus frequency, and the measured frequency will be close, STZX+ tends to perform best with a balance between performance and speed.

b) Amplitude Measurement: Once there is an accurate frequency estimate, it can be used to build the basis vectors for the linear least squares (LLS) fit. Fitting a sinusoidal function with some offset can be done using cosine and sine vectors with the same frequency, and a constant vector. The resulting features matrix is shown in (11) where n is the number of data points in the sampled signal, and N is the measured period of the signal.

$$\mathbf{X} = \begin{pmatrix} 1 & cos(2\pi(0)/N) & sin(2\pi(0)/N) \\ 1 & cos(2\pi(1)/N) & sin(2\pi(1)/N) \\ 1 & cos(2\pi(2)/N) & sin(2\pi(2)/N) \\ \vdots & \vdots & \vdots \\ 1 & cos(2\pi n/N) & cos(2\pi n/N) \end{pmatrix} \tag{11}$$

Using this feature matrix, we can compute a transformation matrix $\mathbf{M}$ by minimizing the residual sum of squares. The result is shown in (12).

$$\mathbf{M} = (\mathbf{X}\mathbf{X}^T)^{-1}\mathbf{X} \tag{12}$$

This can then be cached as needed, and used to compute the weights vector using a single matrix multiplication with the sample vector $\vec{y}$ as shown in (13).

$$\beta = \mathbf{M}\vec{y} \tag{13}$$

Using β, the estimate for y ($\hat{y}$) can be calculated as shown in (14), and used to compute the coefficient of determination (COD) to provide a rough measure of how well the model fits the data.

$$\hat{y} = \beta_0 + \beta_1 cos(...) + \beta_2 sin(...) \tag{14}$$

Since the model consists of the sum of a cosine and sine of the same frequency, we can compute the amplitude of the sinusoid formed by their weighed sum as shown in (15).

$$A_{meas} = \sqrt{\beta_1^2 + \beta_2^2} \tag{15}$$

The final resistance can then be computed using the gain and offset correction factors as discussed in the calibration section, and using the modified version of (7) shown below.

$$R_{dut} = \frac{A_{stim}}{A_{meas}} \cdot G_{nom} \cdot G_{cf} - O_{cf} \tag{16}$$

D. Design Validation

1) Real-Time Flow Validation: For real-time flow validation, a simple test was designed using a microfluidic system. A flow joiner was set up to join three streams. The outer two streams flowed deionized (DI) water (high resistance) at a rate of $90\,\mu L/hr$ while the middle stream was set up to release phosphate buffered saline (PBS) (low resistance) at a rate of $10\,\mu L/hr$. When combined, the system allows the PBS

to form a small stream in the middle third of the chip array, while the DI water on the outer edges remains highly resistive. The DI water used had a conductivity of $64\,\mu S/cm$ and the PBS had a conductivity of $3.4\,mS/cm$ which are different enough to provide noticeable contrast in the image. Spectrum measurements were taken to determine a frequency with good separation. Then samples were taken at that frequency once every 2 seconds in real-time display mode. The DI water was pumping the whole time, whereas the PBS was turned on and off to show the live results. Results are discussed in Section III-B3a.

2) Biofilm Validation: The design validation also was performed by growing a biofilm on the surface of the chip and then looking at the relationship between the resistance measured and the optical coverage of the electrodes. The chip was initially sterilized at $121\,^{\circ}C$ by autoclave. The surface was prepared for bacterial attachment by crosslinking small sheared fragments of DNA (Sigma) at $10\,\mu g/mL$ in 1:1 ratio of water to DNA Binding Buffer (Thermo Fisher). Surface of the chip was incubated at room temperature for 2 hours, and then rinsed with water and dried. Finally, the chip was UV irradiated to crosslink DNA and sterilize growth surface.

Mycobacterium smegmatis was grown in standard 7H9 broth supplemented with 10% OADC and 0.05% Tween-80. Bacteria was grown to an optical density at $600\,nm$ (OD600) of 1.0. Bacteria were washed with RPMI 1640 with 10% FBS and diluted to an OD600 of 0.1. $500\,\mu l$ of bacteria solution was added to the surface of the chip, centered on the electrode array. The chip was then incubated at $37\,^{\circ}C/5\%\,CO_2$ for 24 hours. Media was then replaced with fresh media, and incubated for another 24 hours. In the latest experiment, media was replaced and incubated for another 24 hours to allow for more bacterial growth.

Prior to electrical or optical imaging, the media of the chip was flushed five times using $0.5\,mL$ of fresh media each time, to remove any free-floating bacteria. Flushing was done by tipping the chip slightly and carefully removing the old media on one side then replacing with new media on the other. Clean media was then added to the chip as needed to keep it from running low or drying out, and to ensure that the whole electrode area was covered during measurements.

The chip was then placed on the instrument platform, and a spectrum scan was completed, scanning from $10\,kHz$ to $100\,kHz$ with a stimulus of $100\,mV_{pp}$ on all channels. The results were saved for further analysis. The chip was then removed and prepared for fluorescent imaging.

Biofilm coverage was visualized with LIVE/DEAD BacLight Bacterial Viability Kit (Fisher) as per manufacturer instructions. Live bacteria were stained with SYTO 9 and dead cells or extracellular DNA was stained with propidium iodide.

The imaging was performed using an Olympus BX61W scope with a Hamamatsu Orca2 camera and an Olympus UPlanFLN 4x / 0.13 objective. The initial photos were taken using Metamorph imaging software, and then the photos were stitched together using Photomerge™ Panorama software in planar mode to provide an image of the whole surface of the chip at once.

III. Results

A. Calibration

Each device is slightly different due to process variations in the components. To deal with this, there are three separate calibration steps that need to be run on each device prior to use, to ensure the most accurate results. These can be performed prior to shipping the device to the end user, and the calibration data can be loaded by the software on installation.

1) Zero-Mean Calibration: The stimulus circuit discussed in Section II-B2 has two trim potentiometers (trimpots) designed to allow tuning the circuit so the stimulus DC level is as close to zero as possible. Prior to other calibration of the device, the stimulus must be zero-mean calibrated. The results of calibration on one of the devices is shown in Table II. By using this calibration method, over the full range of stimulus signals, the offset doesn't vary by more than $3\,mV$.

2) Stimulus Voltage Calibration: Calibration of the stimulus voltage is important to get accurate resistance measurements. Calibration is performed automatically through the user interface by sweeping and then measuring the stimulus voltage, and measuring the amplitude using the same algorithm used when measuring resistances. The calibrated stimulus values are within 0.2% of the values manually measured using an external scope during validation. The details are summarized in Table II.

3) Gain/Offset Calibration: Each channel has a slightly different gain error due to feedback resistor variation. There is also a small variation in the series resistance due to varying trace lengths. To compensate for this, and calibrate all the resistance measurements for the device, this requires measurement of a known resistance. The known resistances for all channels are provided by three calibration boards of different values. Each resistance on the board is measured and known. Each board provides a single data point for each channel which can then be fit to compute a gain correction factor (G_{cf}) and an offset correction factor (O_{cf}). Once a calibration board is created, it can be used to calibrate multiple devices, nearly automatically.

To calibrate each new device, a Calibration board with known resistances for all channels is connected, and then calibration readings are taken through the user interface for a minimum of three points per channel. Following calibration, the impedance error is less than 0.7%. The rest of the details are summarized in Table II.

B. Device Validation

1) Noise Performance: The analog front-end noise needs to be low so measurements can be taken over a wider range of resistances. Measurement of the noise performance of the front-end was performed using a Keysight MSOS254A scope to measure the noise spectrum at the input to the ADC when there is no input to a given channel. The spectrum is shown in Fig. 11. The noise characteristics of the instrument are shown in Table II. The measured noise is low enough that it doesn't adversely impact the measurements over the desired operating region.

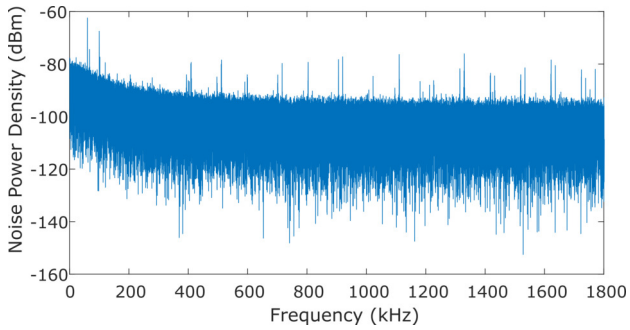

Fig. 11: **Noise Spectrum of Analog Front-End.** This is the measured noise spectrum of the front end which potentially limits how small of a signal can be measured before it gets lost in the noise.

2) Impedance Modulus and Stimulus Range: Impedance modulus accuracy is measured by applying known resistance values to all channels following calibration, and measuring the error between the known value and the measured value over several points in the expected impedance space. The known values are measured using a GwInstek LCR-821 LCR meter, which has an accuracy of 0.05% and 5 significant figures.

Over most of the impedance range, the error is near 0.5%, but it drops at the high end due to poor SNR, and on the low end due to the limitations in front-side voltage swing. For example, with a stimulus of $100\,mV_{pp}$, the accuracy is best over the range $10\,k\Omega$ - $120\,k\Omega$ but drops for values over $500\,k\Omega$ and under $1\,k\Omega$. The possible operating region that maintains a resistance error of less than 1% is shown in Fig. 12. As long as the user keeps the values within these ranges, the resistance values are within the valid calibrated range. Operating slightly outside of this will still give readings, but error may increase slightly. Operating too far outside the range will cause the measurement fit COD to drop below the internal threshold and the device will not give a value and instead will warn the user that the reading is "Out of range". When readings are taken, the user can look at the COD for a given measurement to see the goodness of fit. Summary of the measurement accuracy is included in Table II.

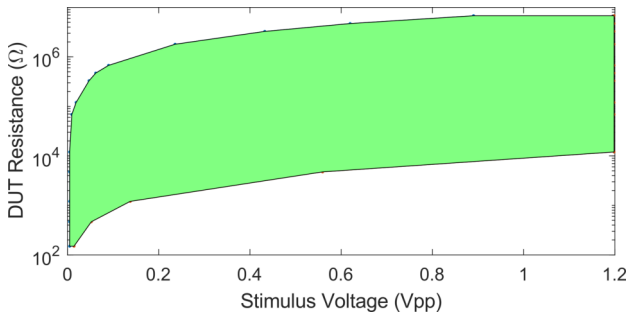

Fig. 12: **Operating Region with Error <1%.** This shows for a given stimulus voltage what range of resistances the device is capable of measuring accurately.

3) Wet Validation Results:

a) Flow Validation: The flow test described in Section III-B3a showed that the device could be used to illustrate the conductivity of the solution change in real-time. When initially PBS is off, the whole system showed high resistance. Turning on the PBS produced the expected small conductive stream down only the middle of the chip as shown in Fig. 13. The teal areas in the image represent high resistance areas. The PBS flow enters on the top middle as evidenced by the lower resistance on the heatmap. As it continues across the array towards the bottom, the PBS solutes diffuse into the DI water, lowering the conductivity of those areas.

TABLE II: Device Measured Specifications

Specification	Value	Unit
Sampling		
Measurement Time per Channel, per Frequency*	1.23	ms
Impedance		
Range @$100\,mV_{pp}$**	1-680	$k\Omega$
Max Error ($10 - 120\,k\Omega$)	0.698	%
Max Error ($1 - 10\,k\Omega$)	1.6521	%
Stimulus		
Stimulus Voltage Range	4.68-1193	mV_{pp}
Stimulus Voltage Resolution	4.68	mV_{pp}
Max V_{pp} Error	0.198	%
Max Offset Error†	12.6	mV
Max Single Quad Offset Error†	3.0	mV
Frequency Range	1-100	kHz
Frequency Resolution	0.093	Hz
Noise††		
Total Noise Power	0.03742	μV^2
Avg. Spectral Density	144.22	$nV/\sqrt{Hz}$
Spot Noise @ $1\,kHz$	814.77	$nV/\sqrt{Hz}$
Spot Noise @ $10\,kHz$	575.05	$nV/\sqrt{Hz}$
Spot Noise @ $500\,kHz$	102.90	$nV/\sqrt{Hz}$
Read Channel		
Bandwidth	159	kHz
Attenuation @ $100\,kHz$	-1.4	dB
Phase Margin	60.	°
Swing	±2.327	V
Power Consumption		
Add-On Only‡	300	mW
Full System‡	1024	mW

* Assuming high confidence mode, worst case USB timing, and 8192 samples/channel
** For full range specifications, see Fig. 12.
† 3σ estimate of maximum
†† This is system noise of the analog front-end. See Fig. 11.
‡ Estimated maximum power under full load

b) Biofilm Validation: The resulting fluorescent image from the biofilm growth experiment described in Section II-D2 is shown in Fig. 14. While the Electrochemical Biosensor System platform can also be used to look at the viability of the cells using a related indicator like oxygen consumption, for this experiment the chip is only used to measure electrode coverage to exercise the new Impedance Spectroscopy Instrument add-on. The surface reflects a fair amount of the emitted green light, so there is a bit of background bleed, but areas with higher coverage still have higher intensities. For the purposes of this experiment, the intensity is a proxy measurement for the biofilm coverage in a given region.

The average green pixel intensities over each electrode region are computed, and then placed into two bins using a threshold in the middle - one bin with high intensity/coverage and one with low intensity/coverage. Using these, we can compare the resistance distributions of these two groups. As

This article has been accepted for publication in a future issue of this journal, but has not been fully edited. Content may change prior to final publication. Citation information: DOI 10.1109/TBCAS.2020.3011918, IEEE Transactions on Biomedical Circuits and Systems

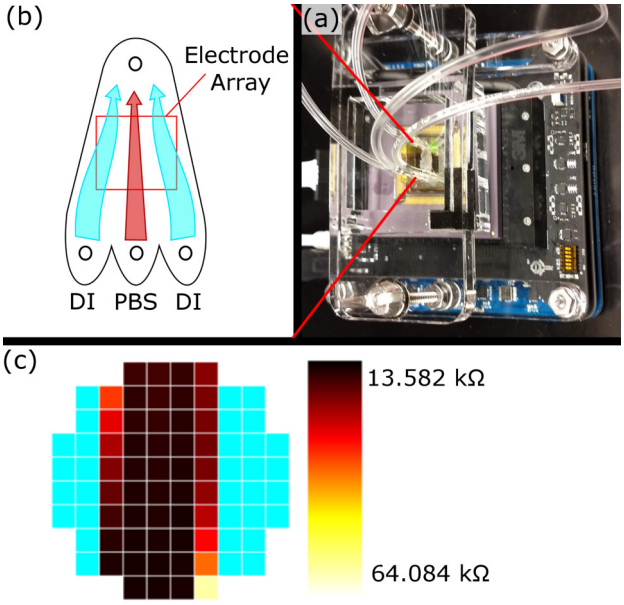

Fig. 13: **Flow Validation Experiment.** (a) Photo of microfluidic setup showing the three inlet tubes and single outlet tube, connected to a shaped flow chamber mounted on the chip surface. (b) Diagram showing the general shape of the flow chamber (not to scale), and how the deionized water (DI) and phosphate buffered saline (PBS) were connected. (c) Example flow image heatmap taken while PBS is pumping.
Note: The heatmap is rotated 180 degrees from how it appeared in the user interface to match the orientation of the other images.

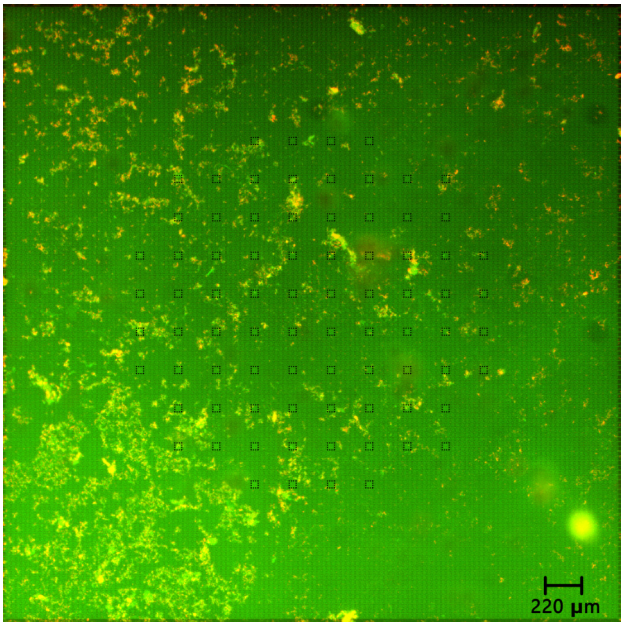

Fig. 14: **Chip Surface with Biofilm Growth and Live/Dead Staining.** The dashed-line boxes outline the impedance electrode locations on the surface of the chip.

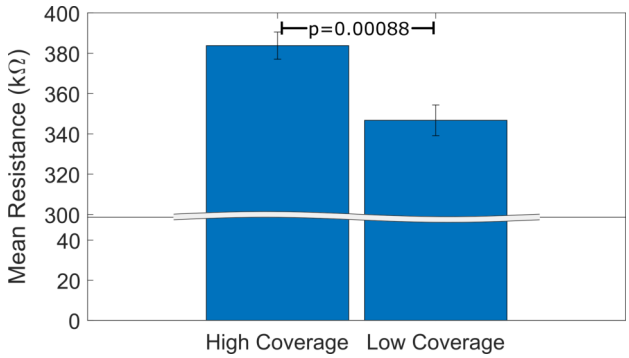

Fig. 15: **Mean Resistance Comparison.** This bar chart divides the electrodes into two groups (high florescent intensity and low florescent intensity) and compares the distributions of the measured resistances.

shown in Fig. 15, the two distributions have different mean resistances (p=0.00088) as expected. The areas with higher coverage have also higher resistance as predicted which can be shown by a linear data fit.

Plotting the green pixel intensity ratio versus the measured resistance gives the result shown in Fig. 16. This data shows the expected positive relation between the intensity and the resistance measured (p=0.000159) although the fluorescent measurements do have a fair amount of variance for this fit $R^2 = 0.303$.

IV. Discussion

The maximum stimulus operating frequency is an important design parameter for EIS. The desired operating frequency range for most of the EIS applications is from several mHz to $100\,kHz$. The connections between the chip and the board introduce additional parasitics that could potentially limit the maximum stimulus frequency of the system. However, the measured bandwidth (excluding the ADC anti-aliasing filter) is $1.5\,MHz$ which is much higher than the desired maximum frequency for the stimulus of $100\,kHz$. The achievable operating frequency range meeting a variety of EIS application requirements is not a concern. Parasitic series resistance is handled via calibration, and all these factors are taken into consideration when determining the operating region (Fig. 12). With the anti-aliasing filter, the system bandwidth going into the ADC is $159\,kHz$ which attenuates higher frequency noise and interference. Additional measurements are provided in Table II.

We would very much like to compare our design with any existing designs that integrate the entire front-end analog interface and the sensors with the back-end digitization and computation. As far as the authors are aware, this is the first attempt to create such a front-to-back integrated system for imaging biofilm coverage. Many existing EIS sensor systems for measuring biofilm coverage are based on single-point measurement using bench-top instrumentation[13], [28], [29]. Even the closest designs in 2D EIS systems we are aware of [14], [20], albeit though they didn't specifically target biofilm coverage, used either a bench-top impedance meter or an off-the-shelf data acquisition card in their measurement system setup, and did not provide much performance data in

This article has been accepted for publication in a future issue of this journal, but has not been fully edited. Content may change prior to final publication. Citation information: DOI 10.1109/TBCAS.2020.3011918, IEEE Transactions on Biomedical Circuits and Systems

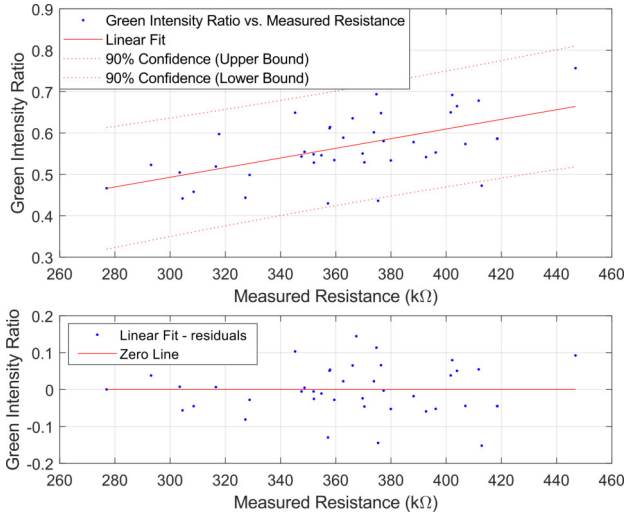

Fig. 16: **Electrode Area Avg. Intensity vs. Resistance.** This plot shows the relation between the measured resistances and the green intensity ratio (top). The bottom shows the residuals from a linear fit.

their papers. Therefore, it is difficult to provide a meaningful performance comparison in this paper.

The evolution of bacteria colonization, the formation of biofilm extracellular polymeric substance (EPS), and the corresponding matrix permeability and their mechanical properties are still not well understood; they are still the focus of continued research efforts[30]. Recent efforts in monitoring biofilm formation and growth using impedance spectroscopy have revealed some interesting findings related to the microenvironment, adhesion, and the continued metabolic process of bacteria in biofilm[31], [32], [33]. The impedance relationship is highly dependent on experiment setup such as the microenvironment, biofilm growth dynamics, and sensor electrode configuration[33]. For our experiment setup with IDEs, Fig. 16 shows a clear positive correlation between the measured resistance and the biofilm coverage measured by the green fluorescence intensity ratio. This relationship is in agreement with similar experimental setups by others using IDEs to measure biofilm growth and coverage [28], [29].

One important feature of our system is the spatial information the system provides compared to many other systems where only single measurement point is available[28], [29], [13]. However, the scatter plots in Fig. Fig. 16 show a significant amount of variation along the trend lines. The variations may be contributed by several sources:

- Different states of adhesion of biofilm on the surface of the chip may result in different impedance readings. When the impedance measurements were taken, the medium in the chamber was kept static. We hypothesize that some colonies on the surface were well adhered to the sensor surface, whereas others may not have been. However, fluorescent intensity does not distinguish colonies that were well adhered from the ones that were not, while impedance measurements would differentiate. Biofilm adhesion and its impact on impedance readings has been recently discussed by Guła et. al. and others[30], [32].
- Different metabolic states of individual colonies may result in different impedance readings. It has been reported by Estrada-Leypon et. al. and others[32], [28] that metabolic process of biofilm colonies can produce slight change in ionic concentrations of the medium within their vicinity. Therefore, different metabolic rates of different colonies may influence impedance readings.
- Fluorescent baseline variations caused by interaction between the light source and the intrinsic fluorescence in many samples either as autofluorescence or as reagent background. Fluorescent intensity reading errors may also contribute to the baseline variations. Saturation of camera sensors, and lens vignetting may also contribute to additional reduced dynamic range and baseline variations in the fluorescent intensity measurements.

There are no known methods to determine whether bacteria colonies are well adhered to the surface or not. It remains a research challenge. However, the integrated sensor system presented in this paper may provide a potential solution to this issue which is discussed as part of the future work in the next section.

V. Conclusions and Future Work

The multichannel impedance spectroscopy device successfully adds impedance sensing capabilities to an advanced CMOS biosensor platform, and opens the doors to many potential studies of biofilm with the capability of obtaining real-time spatial information. The coverage validation using florescence demonstrates the ability of the device to detect various levels of biofilm growth over the surface, and confims a positive relation between biofilm coverage and impedance modulus. The specification validation confirms that the device can operate over the range suitable for EIS that have been used by previous experiments, and it broadens the capabilities allowing further quantitative analyses.

The fact that the integrated CMOS biosensor platform provides both electrochemical sensors[26] and now the EIS sensors densely interlaced in a single package could potentially allow users to detect whether a biofilm colony adheres to the sensor surface. One of our future work goals is to investigate the use of interlaced electrochemical sensors around an EIS sensor to measure medium conditions that would indicate biofilm adhesion. For example, the electrochemical sensors can be used to measure oxygen concentrations within the vicinity of an EIS sensor. When a bacteria colony in a biofilm is well adhered to the surface, it tends to create a more hypoxic microenvironment compared to a colony that does not adhere to the surface. Furthermore, the oxygen sensors would also provide a measure of the metabolism of bacteria colonies giving rise to a novel way to potentially reduce the impedance variations contributed by the first two sources listed in the previous section. Lastly, there have been many efforts to perform fluorescent background signal correction[34], [35]. Some of the existing algorithms can be used in our EIS system to improve fluorescent baseline uniformity.

VI. Acknowledgment

Thanks to Luke Schwerdtfeger for performing the fluorescent imaging, and Dr. Stuart Tobet for providing the equipment. The authors would also like to thank Dr. Andres Obregon Henao for his participation in the initial discussions of the experiments.

References

[1] NIH, "RESEARCH ON MICROBIAL BIOFILMS," 2002. [Online]. Available: https://grants.nih.gov/grants/guide/pa-files/pa-03-047.html

[2] S. Veerachamy *et al.*, "Bacterial adherence and biofilm formation on medical implants: A review," *Journal of Engineering in Medicine*, vol. 228, no. 10, pp. 1083–1099, 2014. [Online]. Available: https://journals.sagepub.com/doi/pdf/10.1177/0954411914556137

[3] J. O'Neill, "Antimicrobial Resistance: Tackling a crisis for the health and wealth of nations," UK Review on Anti-Microbial Resistance, Tech. Rep., 2014. [Online]. Available: https://amr-review.org/sites/default/files/AMR%20Review%20Paper%20-%20Tackling%20a%20crisis%20for%20the%20health%20and%20wealth%20of%20nations.pdf

[4] J. O'Neill, "Tackling Drug-Resistant Infections Globally: Final Report and Recommendations," UK Review on Anti-Microbial Resistance, Tech. Rep., 2016. [Online]. Available: https://amr-review.org/sites/default/files/160525_Final%20paper_with%20cover.pdf

[5] M. Altaf *et al.*, "Evaluation of the Mycobacterium smegmatis and BCG models for the discovery of Mycobacterium tuberculosis inhibitors," *Tuberculosis*, vol. 90, no. 6, pp. 333–337, nov 2010. [Online]. Available: https://linkinghub.elsevier.com/retrieve/pii/S1472979210001034

[6] B. H. Neufeld *et al.*, "Metal-Organic Framework Material Inhibits Biofilm Formation of Pseudomonas aeruginosa," *Advanced Functional Materials*, vol. 27, no. 34, pp. 1–9, 2017.

[7] Q. Yu *et al.*, "In vitro evaluation of tobramycin and aztreonam versus Pseudomonas aeruginosa biofilms on cystic fibrosis-derived human airway epithelial cells," *Journal of Antimicrobial Chemotherapy*, vol. 67, no. 11, pp. 2673–2681, 2012. [Online]. Available: https://academic.oup.com/jac/article-abstract/67/11/2673/713104

[8] D. Nivens *et al.*, "Continuous nondestructive monitoring of microbial biofilms: a review of analytical techniques," *Journal of Industrial Microbiology*, vol. 15, no. 4, pp. 263–276, 1995. [Online]. Available: https://link.springer.com/content/pdf/10.1007{%}2FBF01569979.pdf

[9] G. Chen *et al.*, "Instrumental analysis of microbiologically influenced corrosion," *Biodegradation*, vol. 8, no. 3, pp. 189–200, 1997. [Online]. Available: https://link.springer.com/content/pdf/10.1023{%}2FA{%}3A1008229419434.pdf

[10] Z. Keresztes *et al.*, "Role of redox properties of biofilms in corrosion processes," *Electrochimica Acta*, vol. 46, no. 24-25, pp. 3841–3849, 2001. [Online]. Available: www.elsevier.com/locate/electacta

[11] A. Radu *et al.*, "Diagnostic of functionality of polymer membrane-based ion selective electrodes by impedance spectroscopy," *Analytical Methods*, vol. 2, no. 10, pp. 1490–1498, 2010. [Online]. Available: www.rsc.org/methods

[12] T. Kim *et al.*, "Influence of attached bacteria and biofilm on double-layer capacitance during biofilm monitoring by electrochemical impedance spectroscopy," *Water Research*, vol. 45, no. 15, pp. 4615–4622, oct 2011. [Online]. Available: https://www.sciencedirect.com/science/article/pii/S0043135411003447?via{%}3Dihub

[13] H. Ben-Yoav *et al.*, "An electrochemical impedance model for integrated bacterial biofilms," *Electrochimica Acta*, vol. 56, no. 23, pp. 7780–7786, sep 2011. [Online]. Available: https://www.sciencedirect.com/science/article/pii/S0013468610016579

[14] Y. Chen *et al.*, "CMOS high density electrical impedance biosensor array for tumor cell detection," *Sensors and Actuators B: Chemical*, vol. 173, pp. 903–907, oct 2012. [Online]. Available: https://www.sciencedirect.com/science/article/pii/S0925400512007046

[15] C. Erbay *et al.*, "Three-dimensional porous carbon nanotube sponges for high-performance anodes of microbial fuel cells," *Journal of Power Sources*, vol. 298, pp. 177–183, dec 2015. [Online]. Available: https://linkinghub.elsevier.com/retrieve/pii/S0378775315301750

[16] A. ter Heijne *et al.*, "Quantification of bio-anode capacitance in bioelectrochemical systems using Electrochemical Impedance Spectroscopy," *Journal of Power Sources*, vol. 400, pp. 533–538, oct 2018. [Online]. Available: https://linkinghub.elsevier.com/retrieve/pii/S0378775318308620

[17] X. Dominguez-Benetton *et al.*, "The accurate use of impedance analysis for the study of microbial electrochemical systems," *Chemical Society Reviews*, vol. 41, no. 21, pp. 7228–7246, oct 2012. [Online]. Available: http://xlink.rsc.org/?DOI=c2cs35026b

[18] C. Patel *et al.*, "Combined Spectrophotometric-Electrochemical Impedance Imaging System for Biofilm Research," *Journal of Laboratory Automation*, vol. 10, no. 1, pp. 16–23, 2005. [Online]. Available: https://journals.sagepub.com/doi/pdf/10.1016/j.jala.2004.08.013

[19] B. H. Liu *et al.*, "In situ biosensing of the nanomechanical property and electrochemical spectroscopy of Streptococcus mutans-containing biofilms," *Journal of Physics D: Applied Physics*, vol. 46, no. 275401, 2013. [Online]. Available: https://iopscience.iop.org/article/10.1088/0022-3727/46/27/275401/pdf

[20] A. J. Mason *et al.*, "High-throughput impedance spectroscopy biosensor array chip," *Philosophical Transactions of the Royal Society A: Mathematical, Physical and Engineering Sciences*, vol. 372, no. 2012, 2014. [Online]. Available: http://dx.doi.org/10.1098/rsta.2013.0107

[21] M. Varshney and Y. Li, "Interdigitated array microelectrodes based impedance biosensors for detection of bacterial cells," *Biosensors and Bioelectronics*, vol. 24, no. 10, pp. 2951–2960, jun 2009. [Online]. Available: https://www.sciencedirect.com/science/article/pii/S095656630800571X

[22] J. J. Paredes *et al.*, "Interdigitated microelectrode biosensor for bacterial biofilm growth monitoring by impedance spectroscopy technique in 96-well microtiter plates," *Sensors and Actuators B: Chemical*, vol. 178, pp. 663–670, 2013. [Online]. Available: https://www-sciencedirect-com.ezproxy2.library.colostate.edu/science/article/pii/S0925400513000348

[23] S. Subramanian *et al.*, "An Integrated Microsystem for Real-Time Detection and ThresholdActivated Treatment of Bacterial Biofilms," *ACS Applied Materials & Interfaces*, vol. 9, no. 37, pp. 31 362–31 371, 2017. [Online]. Available: https://pubs-acs-org.ezproxy2.library.colostate.edu/doi/pdf/10.1021%2Facsami.7b04828

[24] R. C. Huiszoon *et al.*, "Flexible Platform for In Situ Impedimetric Detection and Bioelectric Effect Treatment of Escherichia Coli Biofilms," *IEEE Transactions on Biomedical Engineering*, vol. 66, no. 5, pp. 1337–1345, 2019. [Online]. Available: https://ieeexplore-ieee-org.ezproxy2.library.colostate.edu/stamp/stamp.jsp?tp=&arnumber=8477054&tag=1

[25] W. Tedjo *et al.*, "Electrochemical biosensor system using a cmos microelectrode array provides high spatially and temporally resolved images," *Biosensors and Bioelectronics*, vol. 114, pp. 78 – 88, 2018. [Online]. Available: http://www.sciencedirect.com/science/article/pii/S0956566318302720

[26] W. Tedjo and T. Chen, "An integrated biosensor system with a high-density microelectrode array for real-time electrochemical imaging," *IEEE Transactions on Biomedical Circuits and Systems*, November 2019. [Online]. Available: https://ieeexplore.ieee.org/document/8901972

[27] L. Yang and R. Bashir, "Electrical/electrochemical impedance for rapid detection of foodborne pathogenic bacteria," *Biotechnology Advances*, vol. 26, no. 2, pp. 135–150, mar 2008. [Online]. Available: https://www.sciencedirect.com/science/article/pii/S0734975007001176

[28] O. Estrada-Leypon *et al.*, "Simultaneous monitoring of Staphylococcus aureus growth in a multi-parametric microfluidic platform using microscopy and impedance spectroscopy," *Bioelectrochemistry*, vol. 105, pp. 56–64, 2015. [Online]. Available: http://www.sciencedirect.com/science/article/pii/S156753941500064X

[29] J. Bruchmann *et al.*, "Multi-channel microfluidic biosensor platform applied for online monitoring and screening of biofilm formation and activity." *PloS one*, vol. 10, no. 2, p. e0117300, 2015.

[30] N. Billings *et al.*, "Material properties of biofilms-a review of methods for understanding permeability and mechanics." *Reports on progress in physics. Physical Society (Great Britain)*, vol. 78, no. 3, p. 36601, feb 2015.

[31] P. M. D. S. Abrantes and C. W. J. Africa, "Measuring Streptococcus mutans, Streptococcus sanguinis and Candida albicans biofilm formation using a real-time impedance-based system," *Journal of Microbiological Methods*, vol. 169, p. 105815, 2020. [Online]. Available: http://www.sciencedirect.com/science/article/pii/S0167701219309790

[32] G. Guła *et al.*, "The Application of Impedance Spectroscopy for Pseudomonas Biofilm Monitoring during Phage Infection." *Viruses*, vol. 12, no. 4, apr 2020.

[33] J. B. J. H. van Duuren *et al.*, "Use of Single-Frequency Impedance Spectroscopy to Characterize the Growth Dynamics of Biofilm Formation in Pseudomonas aeruginosa." *Scientific reports*, vol. 7, no. 1, p. 5223, jul 2017.

[34] V. Mazet *et al.*, "Background removal from spectra by designing and minimising a non-quadratic cost function," *Chemometrics and Intelligent Laboratory Systems*, vol. 76, no. 2, pp. 121–133,

2005. [Online]. Available: http://www.sciencedirect.com/science/article/pii/S0169743904002412

[35] P. J. Cadusch *et al.*, "Improved methods for fluorescence background subtraction from Raman spectra," *Journal of Raman Spectroscopy*, vol. 44, no. 11, pp. 1587–1595, 2013. [Online]. Available: https://onlinelibrary.wiley.com/doi/abs/10.1002/jrs.4371